






Design of Active Sensing Smart Skin for Incipient Slip Detection in Robotics Applications

Cheng Liu , Tae Myung Huh , Spencer X. Chen , Lingling Lu, Fotis Kopsaftopoulos , Mark R. Cutkosky , and Fu-Kuo Chang

Abstract—Tactile sensing is paramount for robots operating in human-centered environments to help understand interactions with objects. One challenging issue in tactile sensing is the slip detection problem. Currently, most slip detection methods use passive sensors, which only measure force or vibration, but not directly the contact area, which is one of the most reliable parameters for slip detection. Other methods, which do measure contact area such as optical methods often suffer from complex sensor configurations and lack of flexibility for customization. Active sensing, in contrast, has simple sensor configurations, and can also directly measure the contact area to improve the efficiency for slip detection. In this article, a novel active sensing smart skin was developed for incipient slip detection, which leverages piezoelectric transducers as actuators/sensors. First, a robotic fingertip with embedded actuator and sensor was created in which the actuator generates ultrasonic guided waves received by the sensor during a slip scenario. By analyzing the received signals using an attenuation-based method, the entire contact condition evolution can be monitored within 1 ms. Then, an optical method was used to validate the signal attenuation, which correlated consistently with the contact area. Finally, a unique robotic skin was created which demonstrated robust and sensitive response for incipient slip detection.

Index Terms—Active sensing, guided wave, incipient slip detection, piezoelectric transducer, smart skin, tactile sensing.

I. INTRODUCTION

TACTILE sensing aims to assess object properties, e.g., shape, texture, size, or temperature. It is also desired for slip detection, soft object grasping without squeezing, and object shape detection under vision precluded environments. Resembling humans, robots with tactile sensing can improve their ability to interact with objects, depending on their texture, weight, stiffness, temperature, and so on [1], [2], [3]. Tactile sensing is unsurpassed for robots working in human-centered environments. For example, a care-giving robot should be capable of dressing a person, grasping objects in hidden places such as a pocket, and massaging a paralyzed limb to improve blood flow in nerves and tissues. All the tasks require fine manipulation leveraging tactile sensing and cannot be achieved with vision-only sensors. Another simple example is that it is formidably challenging to tie shoes on a cold day when human fingers are numb [4], but a robot's ability to accomplish this task would not be diminished. One challenging issue in robotic tactile sensing is slip detection since the slip mechanics are complicated in nature. Studies [5] have shown that during the onset of tangential slip, the contact area between a human finger and a flat surface reduces. This is also true for humanoid robots, which means measuring the contact area between robot finger and object is the key to detect the incipient slip for robots.

Current methods [6], [7], [8], [9], [10], [11], [12], [13], [14], [15] for slip detection mainly include the following three approaches: 1) To measure the vibrations at the contact surfaces. 2) To measure the force at the contact surfaces. 3) To directly measure the contact area changes. Vibration measurement is a direct reflection of slipping, which leverages its intrinsic dynamic nature. Dynamic sensors such as the accelerometer [14] can be used for this purpose. However, although this method truly measures the status when the slipping is happening, it usually detects the slip too late to avoid it with a closed loop control system [14]. For instance, the integrated piezoelectric vibration tactile sensors [7] can distinguish between static and dynamic friction by measuring the vibration characteristics but are not able to detect incipient slippage early enough to prevent slipping. Another issue of using vibration measurement is that if the sensitivity is high enough to detect the incipient slip for

Manuscript received 20 April 2022; revised 8 August 2022 and 5 October 2022; accepted 19 November 2022. Recommended by Technical Editor J. A. Schultz and Senior Editor G. Alici. This work was supported in part by National Science Foundation and in part by National Robotics Initiative under Grant 1528145. (Corresponding author: Cheng Liu.)

Cheng Liu and Fu-Kuo Chang are with the Department of Aeronautics and Astronautics, Stanford University, Stanford, CA 94305 USA (e-mail: chengliu8@alumni.stanford.edu; fkchang@stanford.edu).

Tae Myung Huh is with the Department of Mechanical Engineering, University of California at Berkeley, Berkeley, CA 94720 USA, and also with the Center for Design Research, Stanford University, Stanford, CA 94305 USA (e-mail: tuhuh@berkeley.edu).

Mark R. Cutkosky is with the Center for Design Research, Stanford University, Stanford, CA 94305 USA (e-mail: cutkosky@stanford.edu).

Spencer X. Chen is with the Department of Aerospace Engineering, University of Michigan, Ann Arbor, MI 48109 USA (e-mail: sxc@umich.edu).

Lingling Lu is with the Key Laboratory for Mechanics in Fluid Solid Coupling Systems, Institute of Mechanics, Chinese Academy of Science, Beijing 100190, China (e-mail: lulingling@imech.ac.cn).

Fotis Kopsaftopoulos is with the Department of Mechanical, Aerospace, and Nuclear Engineering, Rensselaer Polytechnic Institute, Troy, NY 12180 USA (e-mail: kopsaf@rpi.edu).

Color versions of one or more figures in this article are available at <https://doi.org/10.1109/TMECH.2022.3224119>.

Digital Object Identifier 10.1109/TMECH.2022.3224119

fast response to prevent slipping, it will usually detect many “false positive” signals from vibrations in the robot arm and drive train. Force measurement is an indirect way to estimate the slip conditions. For instance, one state-of-the-art force sensor for slip detection is called “BioTac” [6], [12], [13]. Since this sensor measures force, it may require extra effort in computing and large number of datasets to evaluate contact conditions for accurate slip detection. Another example is the capacitive tactile sensor arrays [6], [8], which can directly respond to shear force to detect slip. These sensors are known for their high sensitivity and can achieve over 85% classification rate for incipient slip detection. However, noise coming from temperature, humidity, power supply, and radiation can affect the sensor’s performance. Therefore, the capacitive sensor requires complex circuitry to improve signal-to-noise ratio. Contact area measurement is a direct method for slip detection. It has the advantages of earlier slip detection with less complex computations. However, this method, which is mostly based on the optical mechanisms often have complex sensor configurations and are inflexible to be customized to various robotic hands. For example, the GelSight tactile sensor [9], [10], [11], which is developed by optically measuring contact condition uses an elastomeric slab covered with a reflective membrane. By analyzing the three-dimensional (3-D) shape of the contact object from the sensor signal, it can obtain the information about contact force or slip condition. Unlike other sensors, GelSight directly measures the contact area, which is more informative than measuring only the force or vibration. However, its complex sensor configuration may impede its application to customized robotic hands with complex geometries. To summarize, drawbacks of these current slip detection sensors are as follows:

- 1) Indirect measurement of the contact condition via force or vibration rather than direct reflection of the contact area.
- 2) Complex sensor configuration and inflexibility for customization.
- 3) Necessity of complex circuitry to reduce signal-to-noise ratio.

This is all because contact/slip mechanics over the surface are complicated in nature; hence interpreting data collected from these current sensors surrounding the contact is a highly nonlinear inverse problem in mathematics. It is hardly possible to converge the data into a single unique solution repeatedly.

In contrast to the current slip detection sensing mechanisms, the active sensing [16], [17], [18], [19], [20] method, which actively perturbs the system can provide more information about the sensing target (the contact area). This enriched information, which represents the contact area helps to reduce the uncertainties that originate from this intrinsic nonlinear inverse problem. Therefore, by using the active sensing method, the computational efforts can be reduced due to its direct measurement of the contact area. In addition, typically two lead zirconate titanate (PZT) transducers exchanging ultrasonic waves constitute an active sensing system [16], which means this method also has the advantage of simple sensor configuration and can be easily customized into a variety of complex robotic finger geometries compared with other state-of-the-art sensors. Hence, this active sensing principle, originally designed for aerospace

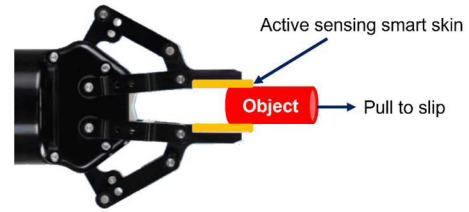


Fig. 1. Definition of incipient slip detection problem in this article with a two-finger gripper robotic hand holding an object.

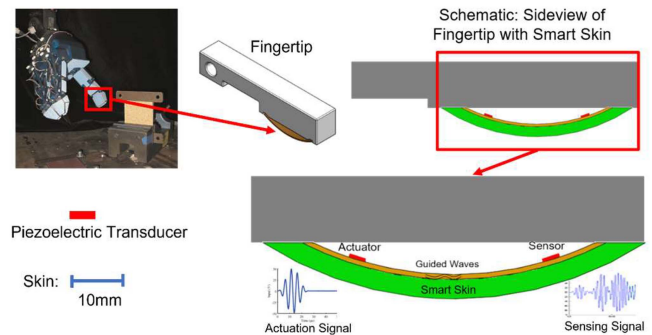


Fig. 2. Design concept of active sensing smart skin on a robotic fingertip.

applications, is adapted here to the specific constraints of robotics. For instance, an active sensing method for thin film gecko-inspired adhesives [17] is developed to detect contact conditions using Lamb waves produced by a pair of piezoelectric strips. The results showed the active sensing method can successfully predict contact failures of the gecko-inspired adhesives.

Therefore, this article aims to apply active sensors that can be easily integrated in a robotic gripper, thereby enabling any robotic arm to detect the incipient slipping of any held object.

II. PROBLEM STATEMENT

Incipient slip detection problem in robotic tactile sensing is still a challenging issue. In this article, the objective is to solve the incipient slip detection problem by using active sensing techniques. More specifically, as shown in Fig. 1, given a two-finger gripper robotic hand holding an object whose weight is constant, and a pulling force that is increasingly applied to this object, it is desired to develop a smart skin embedded with active sensors so that the grippers that can monitor the contact conditions to detect the maximum pulling force that the grippers can resist, before the object slips out of the grippers.

III. METHOD OF APPROACH

We developed an active sensing smart skin system with embedded piezoelectric PZT discs to generate ultrasonic guided waves to measure the contact conditions of the smart skin attached on the robotic fingertip once the skin is in contact with a holding object. The measurement of these contact conditions will then be used for incipient slip detection. This concept is shown in Fig. 2. This active sensing smart system will include the

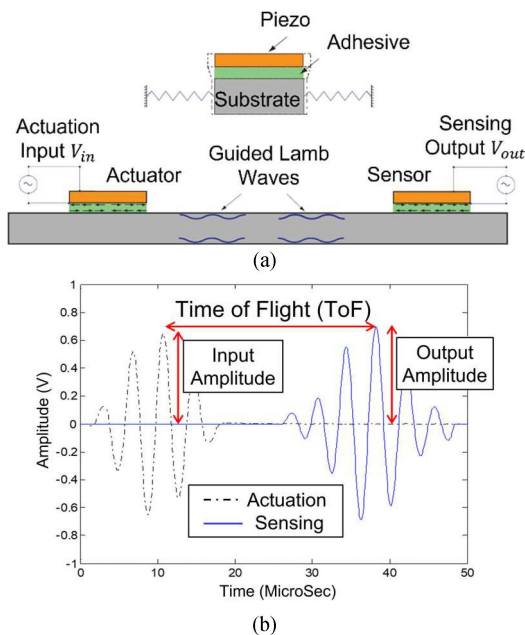


Fig. 3. (a) Schematic of active sensing system. (b) Actuation and sensing signals used in the active sensing system.

PZT discs as both a sensor and an actuator, the unique smart skin, the hardware for signal generation and receiving, and software for data processing.

To achieve this goal, it is desired as follows:

- 1) Develop a diagnostic method using ultrasonic waves to detect incipient slip with PZT active sensors.
- 2) Create an optical experiment with the fingertip to perform slip test to generate needed data to validate the method.
- 3) Design a smart skin with PZTs forming an active sensing system for incipient slip detection with high sensitivity.
- 4) Perform a prototype test on a robotic gripper with an active sensing smart skin system for realizing incipient slip detection.

IV. DIAGNOSTIC METHOD DEVELOPMENT FOR INCIPIENT SLIP DETECTION

A. Active Sensing Using PZTs

The active sensing system consists of two PZT discs: one for actuation and the other for sensing. The actuator will send ultrasonic guided waves through the substrate material. Then, the sensor will receive these waves as output signals. Leveraging both the piezoelectric and inverse piezoelectric effects, we can build the active sensing system [16] by attaching two PZTs onto a substrate. Fig. 3(a) shows a schematic of this system. The PZTs are bonded onto the substrate by a thin layer of adhesive. The active sensing is a three-stage process. The first stage is that the actuator is applied by an electric voltage input, which is converted to induced strain by the piezoelectric actuator. This induced strain is then transmitted through the adhesive layer to the substrate material. This is now inducing the second stage where the guided wave will propagate through the substrate.

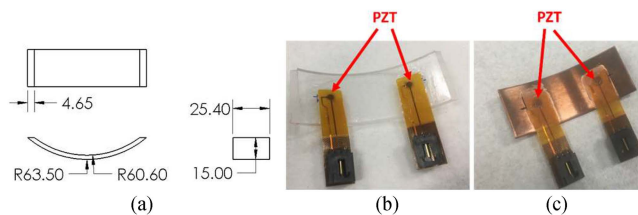


Fig. 4. (a) Dimensions of the acrylic fingertip (units are in mm). (b) Real acrylic fingertip with embedded PZTs. (c) Real copper fingertip with embedded PZTs.

The third stage starts when the sensor receives the guided wave. This sensor will convert the mechanical strains back to electrical output. Fig. 3(b) shows a typical actuation and sensing signal from this active sensing system.

B. Design and Fabrication of Fingertip

With this concept of active sensing, and by mimicking the human finger geometry with a curved shape where it is in contact with the held objects, a customized fingertip was designed. As shown in Fig. 2, the fingertip consists of a curved cylindrical acrylic section with an outer diameter of 127 mm and a thickness of 2.9 mm. The detailed dimensions are depicted in Fig. 4(a). We chose a transparent acrylic as the fingertip material to facilitate the process of validating the change of sensed signals, which is explained in Section V.

To send and receive the ultrasonic guided waves, two single PZT SMART layers manufactured by Acellent Technologies [21] are attached to the back side of the acrylic layer. Because the travel length of the guided wave is short, we chose small PZTs with 3.175 mm in diameter and 0.254 mm in thickness. The distance between two PZTs is 38.1 mm. Fig. 4(b) is the acrylic fingertip with embedded PZTs. The PZTs are bonded to the acrylic layer by using Loctite E-20HP epoxy. Finally, this fingertip is mounted onto a 3D-printed finger to be installed to the slip test setup. In addition to the acrylic fingertip, we also fabricated a copper fingertip with the same outer diameter and a thickness of 1.02 mm. The same type of PZTs were embedded onto the copper layer. Fig. 4(c) shows the copper fingertip. The mechanical material properties of this piezoelectric material as well as its direct piezoelectric matrix [d] and permittivity [e] is the same as in Liu's paper [18]. In both fingertips, one PZT acting as actuator will send ultrasonic guided waves through the acrylic or copper layer to the other sensor. Any perturbation (i.e., slip/touch) along the wave path will reflect on the sensed signal. The received signal is then analyzed for slip detection.

C. Slip Experiment and Data Acquisition

1) *Experimental Setup*: A unique apparatus was designed to aid in the testing of a tactile sensing system using the active sensing method. The apparatus was designed to provide consistent, repeatable measurements under normal and shear loads. The test apparatus is shown in Fig. 5(a) with the computer-aided design (CAD) model. The fingertip is mounted on the low friction pivot of the apparatus. Normal load can be directly added to the

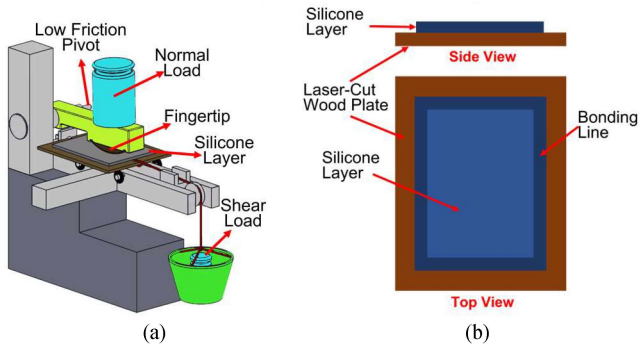


Fig. 5. (a) CAD model of the test setup. (b) Schematic of the wood plate laminated with soft silicone layer.

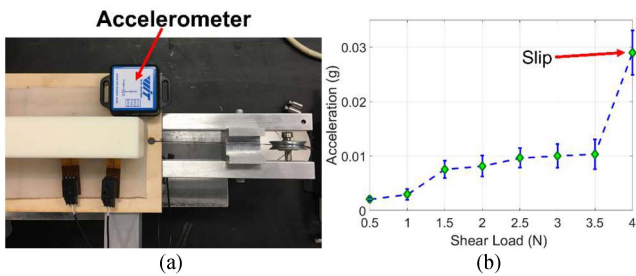


Fig. 6. (a) Accelerometer attached on the wood plate during the slip test. (b) Acceleration at each shear load during a slip test on copper fingertip.

fingertip. A 127 mm \times 102 mm \times 3 mm laser-cut wood plate on the top of which a layer of 102 mm \times 76 mm \times 3 mm soft silicone layer (Smooth-On Ecoflex 00-30 [23]) is laminated rolls across low friction wheels under the finger. Fig. 5(b) demonstrates the boundary conditions between the wood plate and the soft silicone layer. Shear load can be applied to the wood plate to increase the shear load between the fingertip and the soft silicone layer. Shear load can be added until the wood plate slips from the fingertip.

2) *Experimentation Process and Data Acquisition:* We fixed the amount of the normal load to the fingertip while increasing the shear load by a fixed increment before slip happened. After each shear load increment, we actuated the PZT actuator and recorded the sensed signal from the PZT sensor. A series of signals were recorded before and at the shear load increased to the amount when slip happened. These data before slip and at slip were analyzed to predict the onset of dynamic slipping. The determination of slip in our experiment is based on the accelerometer data. As shown in Fig. 6(a), during the test, an accelerometer was attached onto the wood plate to measure its acceleration. Fig. 6(b) shows the acceleration results of five slip tests. At the point of slip, it has a significantly higher acceleration than nonslip states. It is also observed that there is still perceivable acceleration at the loads when slip did not happen. This is due to the mechanical deformation between the copper fingertip and the soft silicone layer during these nonslip loads, which results in this nonzero acceleration.

Fig. 7(a) shows the real test setup, where the normal force was constant at 5 N and shear loads were increasingly applied in 0.5



Fig. 7. (a) Real test setup with copper fingertip. (b) Signal generation and data acquisition system for the slip test setup.

N increments. For the copper fingertip shown in Fig. 7(a), when the shear load increases to 4 N, the onset of the dynamic slip happens. For the acrylic fingertip, when the shear load increases to 3.5 N, the onset of the dynamic slip happens. Each shear load increment was added by gently putting into the cup a 50 g calibration weight. After each increment, we actuated the PZT actuator and recorded the received signal. Signals recorded at zero shear load were taken as the baseline for later signal processing. Fig. 7(b) shows the setup for generating and recording signals. PZTs are actuated with standard tone-burst signal (five-cycle Gaussian with Hanning window) shown in Fig. 7(b) using ScanSentry, a diagnostic hardware platform provided by Acellent Technologies Inc. for Structure Health Monitoring [21]. Excitation frequencies were selected from 200 to 450 kHz with 50 kHz as the frequency step. Sampling frequency for data collection was set at 24 MHz to capture these high frequency signals.

D. Diagnostic Method Development

We obtained sensed signals under different shear level. As mentioned before, the actuation frequencies ranged from 200 to 450 kHz in 50 kHz increments. To determine the diagnostic method for incipient slip detection under different frequencies, we need to analyze the propagation of the guided waves within the fingertip material. In this article, we focused on the fingertip made of acrylic plastic material. In this article, we used DISPERSE [23] software to simulate the Lamb wave propagation in the acrylic material. This material has a thickness of 2.9 mm, density of 1.18 g/cm³, Young's modulus of 3.3 GPa and Poisson's ratio of 0.35. We applied these characteristics in the DISPERSE software to generate the dispersion curve. In addition, we assumed that the curved geometry has limited effects on the wave propagation as compared to a flat plate [24]. Therefore, a flat plate with free boundary conditions is inputted as the definition of material geometry in the software.

Fig. 8(a) shows the dispersion curve of group velocity in the acrylic material. The group velocity is the key parameter to determine the types of modes that the guided wave is traveling with in the material. There are two varieties of the guided waves modes shown in Fig. 8(a): symmetric waves (S_0 , S_1 , and S_2) and antisymmetric waves (A_0 and A_1). At relatively low actuation frequency, which is below 180 kHz, only S_0 mode and A_0 mode exist. However, when the actuation frequency goes higher, multiple modes coexist. Therefore, in our diagnostic analysis,

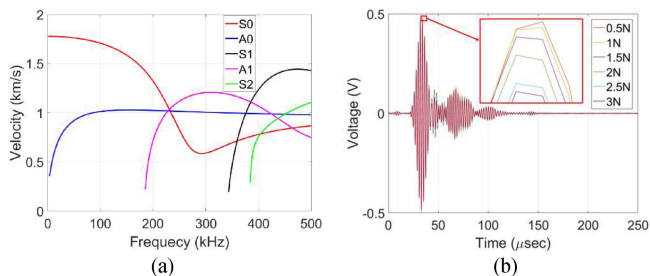


Fig. 8. (a) Dispersion curve of group velocity for acrylic material in the test. (b) Raw sensed signal outputs for each shear load increment at 450 kHz actuation frequency.

the signals will be interpreted from two categories: 1) Signals over low frequency where S_0 and A_0 modes dominate and 2) signals over high frequency where multiple modes exist.

Traditional guided wave based SHM [16] normally focuses on relative lower frequency where there is a distinct S_0 or A_0 mode for analysis, as shown in Fig. 8(a). However, when the geometry of the substrate is too small such as the size of a robotic fingertip, the guided waves will have reflections from the boundaries, which makes it impossible to obtain a clear S_0 or A_0 wave packet. Therefore, in this article, we selected the signals from relative higher frequency, which is 450 kHz. As it is shown in Fig. 8(b), raw signals with 450 kHz actuation frequency under applied shear loads at 0.5 N, 1 N, 1.5 N, 2 N, 2.5 N, and 3 N are recorded, respectively. It is observed that the signal completely decays and has no wave packet existing after 160 μ s. In addition, from Fig. 8(a) the dispersion curve of group velocity in the acrylic material, we can find that there are five different modes coexist, which makes analyzing specific mode difficult at 450 kHz.

Therefore, instead of using specific wave package in certain range of time domain, the long-term signal over the entire time domain [25], [26] was used to characterize the attenuation pattern. The long-term signal can give more accurate attenuation information because it contains all the wave information including the complicated superposition of transmitted and reflected waves [25], [26]. Therefore, the signal energy of the long-term signal is selected as the feature for our diagnostic method. The signal energy is defined as a second norm of the sensor signal in the time domain $[t_s, t_f]$ by the following equation where $V[t]$ represents the discrete sensor signal, ω_s represents the sampling frequency, and t_s and t_f represent the lower and upper bound in time domain

$$E = \frac{2\pi}{\omega_s} \sum_{t=t_s}^{t=t_f} V[t]^2. \quad (1)$$

After calculating received signal energy at each shear load using (1), (2) is applied to obtain each correspondent slip index. The averaged slip indices over 10 tests under each shear load are shown in Fig. 9. One standard deviation of slip indices at 10 tests at contact area is also denoted in this plot. We can observe from the plot that with the increase of the shear load, the slip index accordingly decreases. Note that the amplitude of the noise

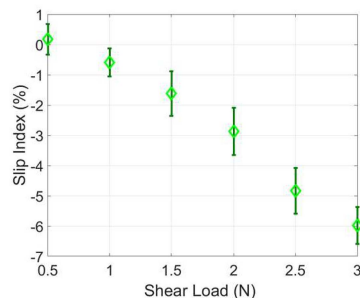


Fig. 9. Slip index at each shear load increment at 450 kHz actuation frequency from the acrylic fingertip.

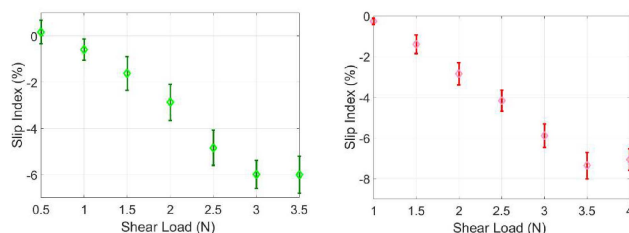


Fig. 10. (a) Acrylic fingertip: Slip index including onset of slip data with actuation frequency at 450 kHz. (b) Copper fingertip: Slip index including onset of slip data with actuation frequency at 450 kHz.

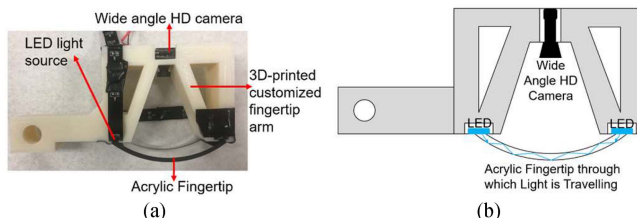


Fig. 11. (a) FTIR sensor configuration including each component. (b) Schematic of the side-view of the FTIR sensor.

floor is merely around 0.2% of the amplitude of the first wave packet in the received signals. This means that the noise level is negligible compared with the slip index change shown in Fig. 9

$$\text{Slip Index} = \frac{E_{\text{Current}} - E_{\text{Baseline}}}{E_{\text{Baseline}}} 100\%. \quad (2)$$

Until now, the focus has been about analyzing the sensed signals before slip happens. When slip does not happen, the shear load between the fingertip and silicone layer is static friction. However, when slip happens, the shear load becomes dynamic friction. Therefore, it is important to know if this transition from static friction to dynamic friction can be captured by using our method, which can then serve as an indicator for incipient slip detection. Fig. 10(a) shows the slip index at 3.5 N when the onset of slip happens from the acrylic fingertip. Note that the data was taken immediately when adding the 3.5 N shear load. It is also noted that out of the 10 tests, we successfully captured five tests to record the sensed signal when the onset of slip happens. As shown, the decreasing trend does not hold any more at 3.5 N

shear load. This can be used to indicate when the incipience of the dynamic slip will happen. This also indicates that during the onset of slip, the trend of the contact condition changes does not hold anymore. Fig. 10(b) shows results from the copper fingertip. It is seen that the result from the copper fingertip demonstrates the same trend as the acrylic fingertip. When the onset of slip happens at 4 N, the trend does not hold, which resembles the results obtained from the acrylic fingertip.

V. VALIDATION OF THE DIAGNOSTIC METHOD

A. Frustrated Total Internal Reflection Experiment

Frustrated total internal reflection (FTIR) [27] is a standard method for obtaining the real area of contact against a smooth, transparent plate. In this method, light will be transmitted inside a layer of transparent material such as the acrylic material. When an external object is in contact with this transparent layer, the change in the index of reflection lets the light to escape. This escaped light will then be captured by a digital camera. This technique has been applied to many applications. It has also been used to measure the positive and negative pressure distributions by the toes of live geckos [27]. In addition, a cylindrical FTIR sensor was implemented to measure the contact area of the gecko elastomer actuator grippers on a curved surface [28]. In this article, a unique FTIR sensor was designed to measure the contact area of the acrylic fingertip against a soft silicone layer under shear loads. The contact area measurement under each shear load was used to validate signal attenuation obtained from the active sensing method.

B. Design and Fabrication of FTIR Sensor

Fig. 11(a) shows the design of the FTIR sensor. It consists of 1) an acrylic fingertip, which has the same geometry used in the active sensing test; 2) A wide angle HD microcamera to capture the contact area between the acrylic fingertip and the silicone layer. 3) A 3D-printed customized fingertip arm, which allows enough shooting distance for the camera; 4) An LED light source, which shoots light into the fingertip. A schematic of the side-view of the FTIR sensor is shown in Fig. 11(b).

C. Slip Experiment With FTIR Sensor

We repeated the same loading procedure as in the active sensing test. At each shear load increment, we recorded the image of the contact area using the wide-angle HD micro camera. We obtained the contact area images under each shear load increment before slip happened. Fig. 12 shows how the FTIR sensor functioned in our test.

After obtaining the images under each shear load, the digital image was processed by decomposing it into red, green, and blue images, respectively. The blue component was selected for postprocessing. Fig. 13(a) shows on the left side the original FTIR images under 0 N shear load condition. The postprocessed image is also shown in Fig. 13(a) on the right side. Fig. 13(b) shows the comparison between the postprocessed images at 0 N shear load and 3 N shear load. It can be observed that there is a

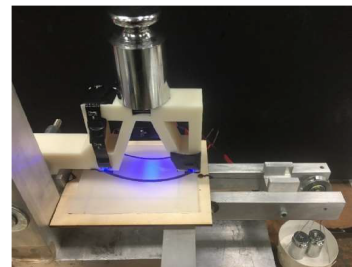


Fig. 12. FTIR sensor in the slip test.

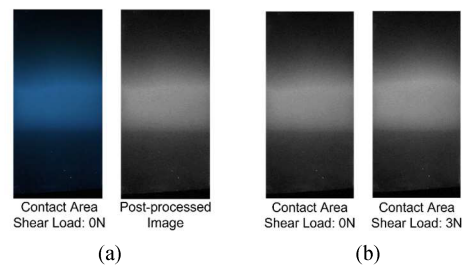


Fig. 13. (a) Selected FTIR images and postprocessed image at 0 N shear load. (b) Contact area comparison: postprocessed image at 0 N shear load VS postprocessed image at 3 N shear load.

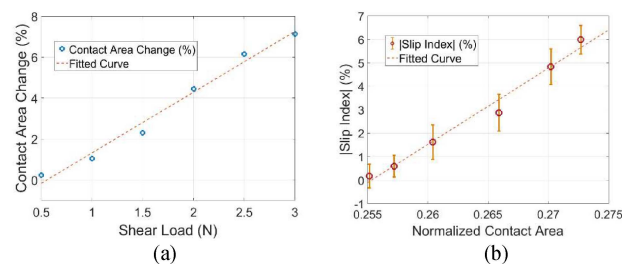


Fig. 14. (a) Contact area change with shear load. (b) Linear relationship between absolute value of slip index and contact area. The dash line is a linear fit between these two parameters.

perceivable growth in the contact area from 0 N shear load to 3 N shear load.

D. Contact Area Calculation and Validation of the Diagnostic Method

Equation (3) was used to quantitatively calculate the contact area for images at each shear load increment including the baseline image where the shear load is zero. This equation essentially calculates the normalized contact area (NCA) for each image

$$NCA = \frac{\text{sum (all pixel color values in the current image)}}{\text{sum (255} \times \text{pixel counts)}}. \quad (3)$$

Fig. 14(a) shows the contact area change calculated using (4) with respect to each corresponding shear load. Fig. 14(a) demonstrates a consistent increasing trend in contact area with

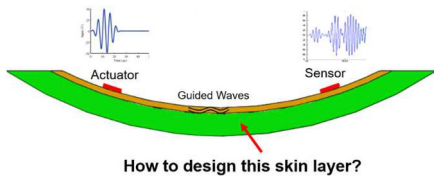


Fig. 15. Design problem of the skin on a copper fingertip for slip detection using active sensing mechanism.

the increment of the shear load

$$\text{Contact Area Change} = \frac{\text{Current NCA} - \text{Baseline NCA}}{\text{Baseline NCA}} 100\%. \quad (4)$$

To validate that the signal attenuation is directly correlated to the contact area, we plotted in Fig. 14(b) the absolute value of the slip index from the acrylic fingertip and the measured contact area at each shear load increment. Each data point corresponds to the absolute average value of slip index and contact area at the same shear load level. The linearly fitted dash line was drawn in Fig. 14(b). A statistical significance test, which is the F test of this regression curve was performed. The F value calculated is 219.87, which is much larger than the designated value, which is 6.61 from the F distribution table. This means this linear regression curve is reliable with the standard 95% confidence bounds. This result further validates that the signal attenuation can directly reflect the contact area change before slip happens. This shows the fact that the signal energy attenuation is directly proportional to the contact area change.

VI. DEVELOPMENT OF THE ACTIVE SENSING SMART SKIN

A. Design Concept of the Smart Skin

1) *Skin Design Criteria:* The previous robust and sensitive results from the copper fingertip in contact with the soft silicone layer inspired us to design a unique skin on robotic fingertip for slip detection. Therefore, our design is based on a substrate material using copper as the substrate for ultrasonic guided wave propagation and a skin material using the soft silicone (Smooth-On Ecoflex 00-30 [22]). As shown in Fig. 15, the design problem is how to design a skin layer that can have a sensitive and robust response to normal and shear loads.

Inspired by the design concept of a tunable and predictable capacitive pressure sensor [29] with the pyramid micro structured dielectric layer, we would develop a new skin based on the following criteria for our situation.

- 1) To adjust to the inherent soft property of the skin material.
- 2) To be compatible with the current fingertip geometry and slip experiment apparatus.
- 3) To be robust and durable loading conditions;
- 4) To enable large mechanical deformation at the skin-copper interface under normal and shear loads, enhancing the attenuation pattern of the ultrasonic guided wave propagation in copper for high sensitivity slip detection.

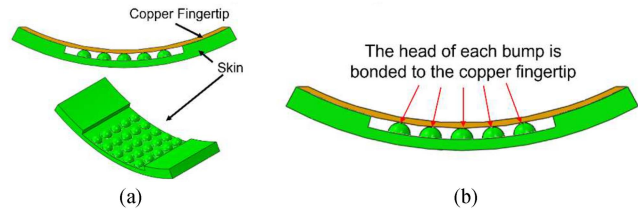


Fig. 16. (a) Design of the skin on a copper fingertip. (b) Head of each bump is bonded to the copper fingertip for mechanical robustness.

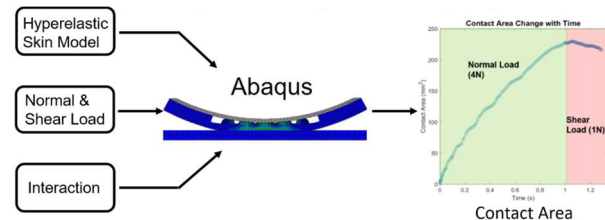


Fig. 17. Overview of our FEM implementation for contact area change analysis at the copper-skin interface.

2) *Design of the Skin Configuration:* Based on the skin design criteria and the fact that the attenuation pattern of the guided wave propagation is closely related to the contact area change caused by the mechanical deformation of the soft silicone material on the copper-silicone interface, a five-by-five hemisphere bump array was designed, as shown in Fig. 16(a). Compared to the pyramid shape, this hemisphere design has the following advantages: 1) it is structurally robust under normal or shear load. 2) It is easy to be fabricated. 3) It allows for sufficient mechanical deformation that can be achieved under both normal and shear loads. The mechanical deformation of the skin will cause large change of the contact area on the copper-skin interface. Hence, it enables its ability to interact with the propagation of the guided waves in the copper. The skin is then bonded to the copper fingertip. To guarantee the mechanical robustness of this skin during various loading conditions, the head of each bump is also bonded to the copper fingertip shown in Fig. 16(b) to enhance consistent deformation during shear loading.

B. Mechanical Analysis of the Skin by Finite Element Method

To quantitatively analyze the contact area change due to different loading conditions at the copper-skin interface, a finite element model was created using ABAQUS 6.12. An overview of this FEM implementation is shown in Fig. 17. The key inputs are the constitutive model for the soft skin material, the loading condition, and the interaction between each component. The output will be the contact area change at the copper-skin interface. This information will then be evaluated to determine if the design of the skin can provide sufficient attenuation for the guided wave signals for high sensitivity slip detection.

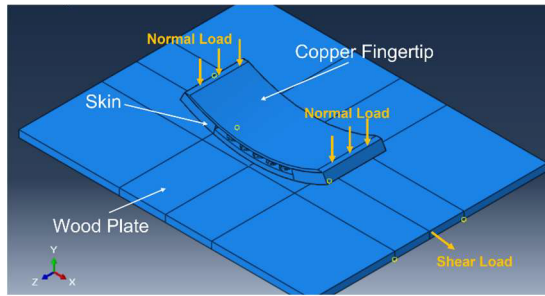


Fig. 18. Finite element model in ABAQUS 6.12 of the experiment including the copper fingertip, skin, and the wood plate.

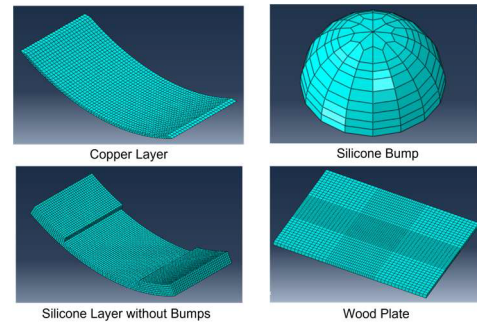


Fig. 20. Mesh of each component in the FEA model.

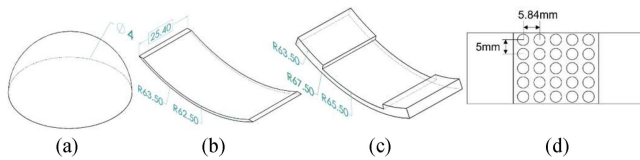


Fig. 19. Dimensions of each component of the fingertip with skin (units are in mm): (a) Bump. (b) Skin without bumps. (c) Copper fingertip. (d) Spacing between each row and column of bumps in the skin.

The detailed model in ABAQUS is shown in Fig. 18. This model consists of a smart skin attached to the copper fingertip and a wood plate in contact with the skin.

The dimensions of each component of the fingertip with skin are shown in Fig. 19. It includes the single bump in Fig. 19(a); the skin without bumps in Fig. 19(b) and the copper fingertip in Fig. 19(c). The spacing between each row and column of bumps are evenly distributed in both directions, as shown in Fig. 19(d). The distance between each bump is specially designed to allow enough space for their mechanical deformation under varying loading conditions. Note that the dimensions of the wood plate in this model are the same as previously described, which are 127 mm \times 102 mm \times 3 mm.

1) *Input Parameter. Material Properties:* To model the hyperelastic property of the soft silicone, the third order reduced polynomial model (Yeoh model) is applied for Ecoflex 0030 [30]. Uniaxial tensile testing on the soft silicone samples has been performed [30] to characterize the parameters which are as follows: $N = 3$; $C_{10} = 5072 \text{ J/m}^3$; $C_{20} = -331 \text{ J/m}^3$ and $C_{30} = -15 \text{ J/m}^3$. The copper has a density of 8.96 g/cm³, Young's Modulus of 128 GPa and Poisson's ratio of 0.33. The wood plate has a density of 0.45 g/cm³, Young's Modulus of 7.2 GPa and Poisson's ratio of 0.33. These parameters are then input into the ABAQUS software.

2) *Input Parameter. Normal and Shear Load:* The static normal and shear load were applied to the fingertip, as shown in Fig. 18. The resultant normal load is 4 N. It is applied evenly at the two edges of the copper fingertip. The shear load applied to the fingertip is up to 1 N. Resembling the test setup, this shear load is applied by pulling the wood plate, as depicted in Fig. 18. The fingertip was confined to move in the Y direction as the mechanical boundary condition. The wood plate was fixed in both Z and Y directions as its mechanical boundary conditions.

3) *Input Parameter. Interactions:* The silicone bumps were connected to the silicone layer using tie constraint. The head of each bump was also tied to the copper. The interaction between the copper and silicone was defined in both tangential and normal directions: the tangential behavior had a friction coefficient of 0.8 based on the previous test results, and the normal behavior was set as "Hard" contact. The interaction between the silicone and wood plate was also defined in both tangential and normal directions: the tangential with a friction coefficient of 1 [31], and the normal was set as "Hard" contact.

4) *Mesh for Each Component in the Model:* The mesh of each component is shown in Fig. 20. Structured mesh was applied to all the components in this model. The C3D8RH elements were applied to model the silicone skin to ensure its ability to simulate large deformation. The C3D8R elements were used both for the copper fingertip and the wood plate. Convergence study has been performed based on the simulated stiffness of the skin. Mesh size has been consistently reduced until the simulated stiffness of the skin converges into a single value. Therefore, the following mesh size for each component has been selected: the mesh size of the bumps was set to 0.25 mm while the silicone layer without bumps was set to 0.75 mm. The mesh size of the copper fingertip was 1 mm while the minimum mesh size for the plate was 2 mm at the center where it is in contact with the skin.

5) *Execution:* A two-step static general analysis was performed. The first step is to apply the normal load of 4 N to the fingertip to press the fingertip down to the wood plate. Keeping the normal force constant at 4 N, the second step is to apply a pulling force of 1 N to the wood plate, which acts as the shear force from the plate to the fingertip. The stable time increment for this simulation is on the order of 1×10^{-6} s.

6) *Simulation Results:* The deformed shape after the first step and second step are shown in Fig. 21, respectively.

The key information to extract is the contact area change at the copper-silicone interface. This interface is highlighted on the top left corner of Fig. 22. Fig. 22 demonstrates the relationship between this contact area change with respect to the applied normal and shear loads.

As shown in Fig. 22(a), at the first step when normal load reaches 4 N, the contact area arrives at the maximum value, which is 228 mm². During the second step in Fig. 22(b) where the normal load stays at 4 N and shear load is gradually increased

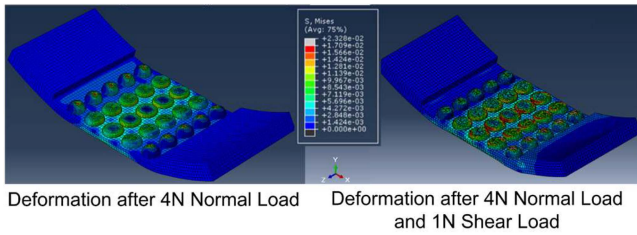


Fig. 21. Mechanical deformation of the silicone skin after normal and shear loads, respectively.

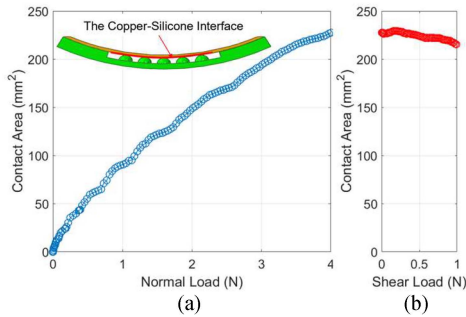


Fig. 22. Relationship between the copper-silicone contact area change with respect to applied normal and shear loads. (a) Step 1: contact area versus normal load. (b) Step 2: contact area versus shear load while normal load stays at 4 N.

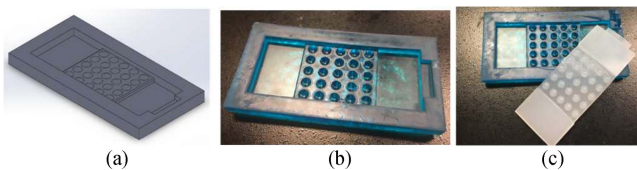


Fig. 23. (a) CAD model of the mold for fabrication of the skin. (b) Three-dimensional printed mold for fabrication of the skin. (c) Soft silicone skin released from the 3D-printed mold.

to 1 N, the contact area decreased to 215 mm². This decreasing slope means that 1 N shear load can cause 6% contact area decrease. Based on the previous results that a 7% contact area change can cause 6% signal attenuation, this amount of decrease in contact area is sufficient to produce perceivable attenuation in guided wave propagation in the copper fingertip. Therefore, this design is proved to be sensitive to shear load sensing and slip detection.

C. Fabrication of the Skin

To fabricate the skin, a mold was created in SOLIDWORKS 2017 shown in Fig. 23(a) and then 3D-printed using the Form two printer from Formlabs. Fig. 23(b) demonstrates the 3D-printed mold. The soft silicone skin was then cured and released from the mold, as shown in Fig. 23(c).

The skin was then bonded to the copper fingertip using Sil-Poxy [32]. This Sil-Poxy has a tear strength of 17.51 N/mm, which is durable for the skin design. Because each bump can share the global shear load, the actual shear load for each bump

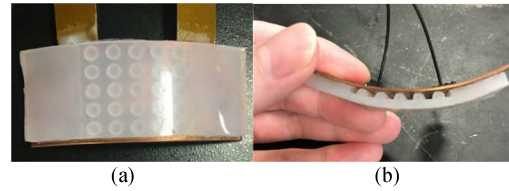


Fig. 24. Copper fingertip laminated with the skin. (a) Front view. (b) Side view.

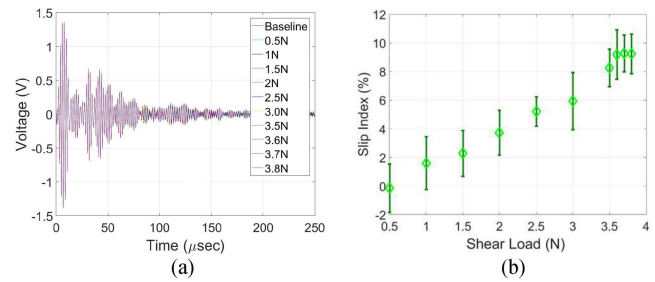


Fig. 25. (a) Raw sensed signal output at 550 kHz actuation frequency. (b) Slip index with respect to shear load for the fingertip with skin.

is on the order of 0.1 N. Therefore, this load level is way below the tear strength of the Sil-Poxy so that this design is durable for our application. We have performed about 50 shear tests on this fingertip with smart skin, and found the performance persists. The copper fingertip with skin was shown in Fig. 24(a) with the front view and in Fig. 24(b) with the side views. This fingertip with the silicone skin was then mounted to our test setup for our experiment.

D. Experiment and Results of the Skin

This new fingertip with skin was mounted to the test setup shown in Fig. 7(a). The normal force was fixed, and shear load was added up to 3.5 N in 0.5 N increments. After reaching 3.5 N, we decreased the increment to 0.1 N up until a shear load of 3.8 N. When the shear load reached 3.9 N, the plate slipped from the fingertip. Again, after each shear load increment, signals from the sensor were recorded. For this fingertip with skin, we leverage the same diagnostic method, and the signals at 550 kHz provided the most robust and sensitive results, which further validates our previous study that this method prevails over higher actuation frequencies. The sensed signals at 550 kHz actuation frequency are plotted in Fig. 25(a). Again, we can see a complete decaying of the signals before 200 μ s. By using (2), the slip index was obtained with respect to shear load, which is shown in Fig. 25(b). This plot is based on the average and standard deviation of five tests. It is observed that the signal energy increases by 10% at around 4 N shear load, which shows great sensitivity to the shear load. This is also consistent with previous study where the increase in contact area correlates with a decrease in sensed signal energy. While in this case, we have the inverse where the decrease in contact area demonstrates the increase in sensed signal energy. Another critical feature

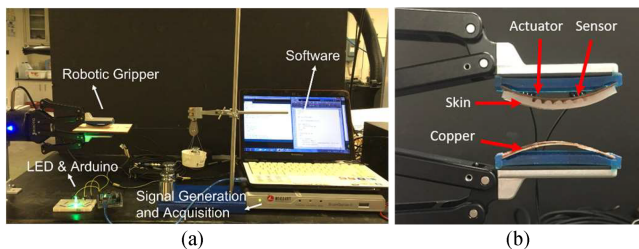


Fig. 26. (a) Overview: an LED slip alert system on a robotic gripper. (b) Design of customized fingertips mounted on a commercial robotic gripper.

in Fig. 25(b) is that close to slip, the slope of this curve alters, which can be used as an indicator for slip detection.

VII. PROTOTYPE ON A ROBOTIC GRIPPER

A. Overview: a LED Slip Alert System on a Robotic Gripper and Test Procedure

Building upon the abovementioned investigation, a LED slip alert system was created to demonstrate this smart skin into a real application. Fig. 26(a) is an overview of this system including the following:

- 1) Robotic gripper (ROBOTIQ 2F-140 Wide Stroke Adaptive Gripper) mounted with the customized fingertip.
- 2) Hardware: A signal generation and data acquisition system for the PZT active sensing.
- 3) Software: A MATLAB script that analyzed the received signal and calculated the slip index.
- 4) An Arduino code that read the software's output from the MATLAB code and controlled the LED connected to the Arduino Uno board.

To apply our active sensing method, two customized fingertips were mounted onto a commercial robotic gripper (ROBOTIQ 2F-140). Fig. 26(b) shows that the upper fingertip consists of a copper with the skin; the bottom fingertip is a pure copper layer. The test procedure includes the following: 1) A user picks up an object. 2) The robotic gripper grasps the object. 3) The user pulls the object from the robotic hand by adding a shear load to the object. The PZT sensors on the top finger senses the incoming slip and alerts the user with a red LED by processing the guided wave signals.

B. Hardware and Software for the Slip Alert System

The hardware for this slip alert system should generate and receive ultrasonic guided wave signals. Based on the selected actuation frequency in this article, the hardware should actuate and receive signals with frequencies above 0.5 MHz.

In this system, the algorithm will run the current data at the corresponding shear load increment and then calculate the slip index using the baseline data, which corresponds to zero shear load status. Taking the current slip index calculated at time t_i , the algorithm will then compare it with the previous slip index at t_{i-1} and calculate the slope based on (5). If the slope is greater than zero, then the algorithm will send signal to light up green

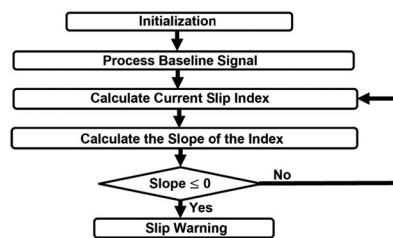


Fig. 27. Flow chart of the software for slip alert system.

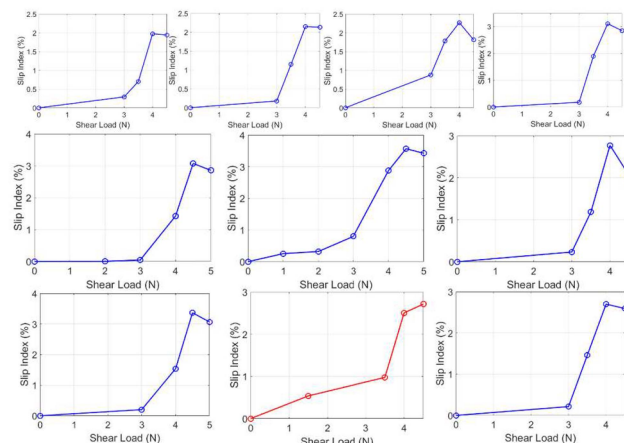


Fig. 28. In total, 10 test results from the robotic gripper: Slip index with respect to shear load before slipping.

LED, which indicates no slip or safe status. If the slope is equal or less than zero, the algorithm will trigger the red LED light, which indicates slip will happen in the next few shear load increments. The flow chart of this software is shown in Fig. 27

$$\text{Slope} = \frac{\text{Slip Index } (t_i) - \text{Slip Index } (t_{i-1})}{\text{Slip Index } (t_{i-1})}, \text{ where } i \geq 2. \quad (5)$$

C. Prototype Test Results

We performed 10 tests on this system. In total, 9 out of 10 tests successfully informed us with the slip alert before the slip happened. The received signals resemble the pattern shown in Fig. 25(b), which has a time length of merely 250 ms. Considering this short amount of time to capture the signal as well as the time consumed to process the signal, the total time to determine one slip index can be within 1 ms. The slip index curves before slip for the 10 tests are shown in Fig. 28. It is perceivable from these figures that 9 out of the 10 test curves' slopes altered close to slip, which agrees with the previous criterion for slip warning shown in Fig. 27. This 90% successful rate further validates the robustness of our method in the application of early slip detection.

In addition, to test our approach on different objects, we have performed the slip tests on three sandpapers with different surface roughness including grit sizes: 1000, 2000, and 3000,

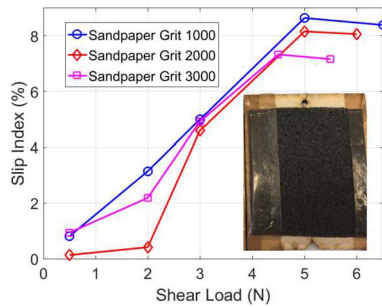


Fig. 29. Test results from different contact objects: three sandpapers with different surface roughness.

respectively. The test sample was shown in Fig. 29. The slip index curves had the same slope change before slip happened, which demonstrates their ability for early slip detection. Conclusively, considering skin's simple sensor configuration and its good sensitivity to shear load, our technology has great potential to be applied into real world robotic applications.

VIII. CONCLUSION

In this article, we presented a novel active sensing smart skin technique using ultrasonic guided waves generated from PZTs. We first designed two fingertips made of acrylic and copper, respectively, both embedded with PZTs. We then tested the fingertip during a slip scenario. Based on the received signals, we developed an attenuation-based method, which can successfully monitor the contact area change before slip happens. Built on these findings, a unique smart skin, which was made of soft silicone material was designed. Finally, a LED slip alert system on a robotic gripper was developed using the active sensing smart skin. The accuracy using our smart skin design for incipient slip detection reached 90% with a 1 ms response time. This fast response time and the superiority of our method compared with other sensors are because: 1) Direct reflection of the contact area rather than indirect measurement of the contact condition via force or vibration. 2) The physics of ultrasonic guided wave signals: the length of the signal is merely 200 ms. 3) Extremely high sampling frequency for data collection: 24 MHz. 4) Simple but robust signal processing algorithm: simply calculate the signal energy, which reflects the contact area for slip detection without relying on complex model training processes. In addition, owing to the simple sensor configuration, our method can be flexible for customization in various robot design. Finally, the signal generation and data acquisition are quite mature to guarantee a high signal-to-noise ratio without extra effort in designing and fabricating complex circuitry for signal conditioning.

Furthermore, one major concern of using active sensing is the power consumption issue compared with other sensing mechanisms. In order to overcome this problem, we can apply the strategy that this active system is not necessarily on all the time, and the triggering of the active sensing can be initiated via the use of event-driven visual sensors or even passive sensors such as strain gauges, capacitive sensors, or other available sensor types for the detection of a potential initial contact.

Future work will focus on applying the smart skin in grasping soft objects that deform under external pressure. In addition, for comprehensive slip evaluation we will need to further investigate our method when contact is actively slipping and experiencing stick-slip.

ACKNOWLEDGMENT

The authors would like to thank Dr. D. Gao for his insights through scientific discussions to this project, like to thank D. Wright in contributing part of the slip test setup at the initial stage of this project, and also like to thank Mr. E. Kuribayashi for gift funding of Kaneka.

REFERENCES

- [1] R. S. Dahiya, G. Metta, M. Valle, and G. Sandini, "Tactile sensing-from humans to humanoid," *IEEE Trans. Robot.*, vol. 26, no. 1, pp. 1–20, Feb. 2010.
- [2] M. R. Cutkosky, R. D. Howe, and W. R. Provancher, "Force and Tactile Sensors," in *Springer Handbook of Robotics*, B. Siciliano and O. Khatib, Eds. Berlin, Germany: Springer, 2008, pp. 455–476.
- [3] S. C. Jacobsen, J. E. Wood, D. F. Knutti, and K. B. Biggers, "The UTAH/M.I.T. Dextrous hand: Work in progress," *Int. J. Robot. Res.*, vol. 3, no. 4, pp. 21–50, 1984.
- [4] R. S. Johansson and J. R. Flanagan, "Coding and use of tactile signals from the fingertips in object manipulation tasks," *Nature Rev. Neurosci.*, vol. 10, no. 5, pp. 345–359, May 2009.
- [5] B. Delhay, P. Lefevre, and J.-L. Thonnard, "Dynamics of fingertip contact during the onset of tangential slip," *J. Roy. Soc. Interface*, vol. 11, no. 100, Nov. 2014.
- [6] B. Heyneman and M. R. Cutkosky, "Slip classification for dynamic tactile array sensors," *Int. J. Robot. Res.*, vol. 35, no. 4, pp. 404–421, Apr. 2016.
- [7] S. Kosaka, M. Nakajima, T. Fukuda, and H. Matsuura, "Slipping detection with integrated piezoelectric vibration tactile sensors," in *Proc. IEEE/SICE Int. Symp. Syst. Integration*, 2008, pp. 111–116.
- [8] X. A. Wu, T. M. Huh, A. Sabin, S. A. Suresh, and M. R. Cutkosky, "Tactile sensing and terrain-based gait control for small legged robots," *IEEE Trans. Robot.*, vol. 36, no. 1, pp. 15–27, Feb. 2020.
- [9] W. Yuan, S. Dong, and E. H. Adelson, "GelSight: High-Resolution robot tactile sensors for estimating geometry and force," *Sensors*, vol. 17, no. 12, Dec. 2017, Art. no. 2762.
- [10] S. Dong, W. Yuan, and E. H. Adelson, "Improved GelSight tactile sensor for measuring geometry and slip," in *Proc. IEEE Int. Conf. Intell. Robots Syst.*, 2017, pp. 137–144.
- [11] J. Li, S. Dong, and E. Adelson, "Slip detection with combined tactile and visual information," in *Proc. IEEE Int. Conf. Robot. Automat.*, 2018, pp. 7772–7777.
- [12] Z. Su et al., "Force estimation and slip detection/classification for grip control using a biomimetic tactile sensor," in *Proc. IEEE-RAS Int. Conf. Humanoid Robots*, 2015, pp. 297–303.
- [13] Z. Su, J. A. Fishel, T. Yamamoto, and G. E. Loeb, "Use of tactile feedback to control exploratory movements to characterize object compliance," *Front. Neurobot.*, vol. 6, pp. 7–7, 2012.
- [14] R. Fernandez, I. Payo, A. S. Vazquez, and J. Becedas, "Slip detection in robotic hands with flexible parts," in *Proc. 1st Iberian Robot. Conf.*, 2013, pp. 153–167.
- [15] D. Gunji et al., "Grasping force control of multi-fingered robot hand based on slip detection using tactile sensor," in *Proc. IEEE Int. Conf. Robot. Automat.*, 2008, pp. 2605–2610.
- [16] J.-B. Ihn and F.-K. Chang, "Pitch-catch active sensing methods in structural health monitoring for aircraft structures," *Struct. Health Monit.-Int. J.*, vol. 7, no. 1, pp. 5–19, Mar. 2008.
- [17] T. M. Huh et al., "Active sensing for measuring contact of thin film gecko-inspired adhesives," *IEEE Robot. Automat. Lett.*, vol. 3, no. 4, pp. 3263–3270, Oct. 2018.
- [18] C. Liu, Y. Zhuang, A. Nasrollahi, L. Lu, M. F. Haider, and F.-K. Chang, "Static tactile sensing for a robotic electronic skin via an electromechanical impedance-based approach," *Sensors*, vol. 20, no. 10, May 2020.

- [19] D. Gao, Z. Wu, L. Yang, and Y. Zheng, "Integrated impedance and Lamb wave-based structural health monitoring strategy for long-term cycle-loaded composite structure," *Struct. Health Monit.-Int. J.*, vol. 17, no. 4, pp. 763–776, Jul. 2018.
- [20] M. Shikida, T. Shimizu, K. Sato, and K. Itoigawa, "Active tactile sensor for detecting contact force and hardness of an object," *Sensors Actuators Phys.*, vol. 103, no. 1/2, pp. 213–218, Jan. 2003.
- [21] A. technologies, "Acellent technologies." Accessed: Nov. 25, 2022. [Online]. Available: <https://www.acellent.com/>
- [22] J. L. Sparks et al., "Use of silicone materials to simulate tissue biomechanics as related to deep tissue injury," *Adv. Skin Wound Care*, vol. 28, no. 2, pp. 59–68, Feb. 2015.
- [23] B. Pavlakovic, M. Lowe, D. Alleyne, and P. Cawley, "Disperse: A general purpose program for creating dispersion curves," in *Review of Progress in Quantitative Nondestructive Evaluation*. Berlin, Germany: Springer, 1997, pp. 185–192.
- [24] V. Giurgiutiu, L. Yu, and D. Thomas, "Embedded ultrasonic structural radar with piezoelectric wafer active sensors for damage detection in cylindrical shell structures," in *Proc. 45th AIAA/ASME/ASCE/AHS/ASC Structures Struct. Dyn. Mater. Conf.*, 2004.
- [25] J. Y. Yang and F. K. Chang, "Detection of bolt loosening in C-C composite thermal protection panels: I. Diagnostic principle," *Smart Mater. Structures*, vol. 15, no. 2, pp. 581–590, Apr. 2006.
- [26] J. K. Yang and F. K. Chang, "Detection of bolt loosening in C-C composite thermal protection panels: II. Experimental verification," *Smart Mater. Structures*, vol. 15, no. 2, pp. 591–599, Apr. 2006.
- [27] E. V. Eason, E. W. Hawkes, M. Windheim, D. L. Christensen, T. Libby, and M. R. Cutkosky, "Stress distribution and contact area measurements of a gecko toe using a high-resolution tactile sensor," *Bioinspiration Biomimetics*, vol. 10, no. 1, Feb. 2015.
- [28] P. Glick, S. A. Suresh, D. Ruffatto, M. Cutkosky, M. T. Tolley, and A. Parness, "A soft robotic gripper with gecko-inspired adhesive," *IEEE Robot. Automat. Lett.*, vol. 3, no. 2, pp. 903–910, Apr. 2018.
- [29] S. R. A. Ruth, L. Beker, H. Tran, V. R. Feig, N. Matsuhsu, and Z. Bao, "Rational design of capacitive pressure sensors based on pyramidal microstructures for specialized monitoring of biosignals," *Adv. Funct. Mater.*, vol. 30, no. 29, Jul. 2020.
- [30] Y. Elsayed et al., "Finite Element Analysis and Design Optimization of a Pneumatically Actuating Silicone Module for Robotic Surgery Applications," *Soft Robot.*, vol. 1, no. 4, pp. 255–262, Dec. 2014.
- [31] F. Xu, K.-i. Yoshimura, and H. Mizuta, "Experimental study on friction properties of rubber material: Influence of surface roughness on sliding friction," *Procedia Eng.*, vol. 68, pp. 19–23, 2013.
- [32] N. S. Hoang, B. H. Ge, and W. T. Kuo, "Developing and Evaluating a Simulator for Complex IVC Filter Retrieval," *Academic Radiol.*, vol. 27, no. 6, pp. 885–888, Jun. 2020.



Cheng Liu received the B.S. degree in aerospace engineering from the Nanjing University of Aeronautics and Astronautics, Nanjing, China, in 2013, and the M.S. degree in aeronautics and astronautics and the Ph.D. degree in mechanical engineering from Stanford University, Stanford, CA, USA, in 2015 and 2015, respectively.

His research interests include smart materials and structures, robotic tactile sensing, and structural health monitoring.



Tae Myung Huh received the B.S. degree from Seoul National University, Seoul, South Korea, in 2014, and the M.S. and Ph.D. degrees from Stanford University, Stanford, CA, USA, in 2016 and 2020, respectively, all in mechanical engineering.

He is currently a Postdoctoral Researcher with the University of California, Berkeley, CA, USA. His research interests include tactile/force-torque sensors, bioinspired robots, sensor networks, and perception of grasping.



Spencer X. Chen received the B.S.E. degree in aerospace engineering from the University of Michigan, Ann Arbor, MI, USA, in 2020.

He is currently working in the aerospace industry as a Software Engineer developing autopilot systems. His research interests include autonomous aircraft, smart materials, and aeroelasticity.



Lingling Lu received the Ph.D. degree in engineering mechanics from the Institute of Mechanics, Chinese Academy of Sciences, Beijing, China, in 2014.

She is currently an Associate Professor with the Institute of Mechanics, Chinese Academy of Sciences. Her research interests include structural health monitoring, structural Intelligent perception, damage identification, and load identification.



Fotis Kopsaftopoulos received the Ph.D. degree in mechanical and aeronautical engineering from the University of Patras, Patras, Greece, in 2012.

He is currently an Assistant Professor with the Department of Mechanical, Aerospace, and Nuclear Engineering, Rensselaer Polytechnic Institute, Troy, NY, USA. His research interests include intelligent structural systems, structural health monitoring diagnostics and prognostics, stochastic system identification and machine learning, fly-by-feel aerial vehicles, bioinspired systems, and smart materials and structures.



Mark R. Cutkosky received the Ph.D. degree in mechanical engineering from Carnegie Mellon University, Pittsburgh, PA, USA, in 1985.

He is currently the Fletcher Jones II Professor with the Department of Mechanical Engineering, Stanford University, Stanford, CA, USA. His research interests include robotic manipulation and tactile sensing, and the design and fabrication of biologically inspired systems.

Dr. Cutkosky is a former Fulbright Chair, Anderson Faculty Scholar, and NSF Presidential Young Investigator. He is a member of the American Society of Mechanical Engineers.



Fu-Kuo Chang received the Ph.D. degree in mechanical engineering from the University of Michigan, Ann Arbor, MI, USA, in 1983.

He is currently a Professor with the Department of Aeronautics and Astronautics, Stanford University, Stanford, CA, USA. He is currently involved in design on smart skins for robots, crashworthiness analysis of composite structures, and structural health monitoring and management for composite materials. His recent research interests include design of bioinspired sensory materials for fly-by-feel autonomous vehicle, smart adhesives and intelligent composites, and robust multifunctional battery chassis systems for automotive applications.